A New Map of the Permafrost Distribution on the Tibetan Plateau

Defu Zou[1, 2], Lin Zhao[1], Yu Sheng[2], Ji Chen[2], Guojie Hu[1], Tonghua Wu[1], Jichun Wu[2], Changwei Xie[1], Xiaodong Wu[1], Qiangqiang Pang[1], Wu Wang[1], Erji Du[1], Wangping Li[1], Guangyue Liu[1], Jing Li[2], Yanhui Qin[1], Yongping Qiao[1], Zhiwei Wang[1], Jianzong Shi[1] and Guodong Cheng[2]

5   [1]Cryosphere Research Station on Qinghai–Xizang Plateau, State Key Laboratory of Cryospheric Science, Northwest Institute of Eco–Environment and Resources, Chinese Academy of Sciences (CAS), Lanzhou, 730000, China
[2]State Key Laboratory of Frozen Soil Engineering, Northwest Institute of Eco–Environment and Resources, CAS, Lanzhou, 730000, China

Correspondence to: L. Zhao (linzhao@lzb.ac.cn)

10   **Abstract.** The Tibetan Plateau (TP) possesses the largest areas of permafrost terrain in the mid- and low-latitude regions of the world. A detailed database of the distribution and characteristics of permafrost is crucial for engineering planning, water resource management, ecosystem protection, climate modelling, and carbon cycle research. Although some permafrost distribution maps have been compiled in previous studies and have been proven to be very useful, due to the limited data source, ambiguous criteria, little validation, and the deficiency of high-quality spatial datasets, there is high

15   uncertainty in the mapping of the permafrost distribution on the TP. In this paper, a new permafrost map was generated based on freezing and thawing indices from modified Moderate Resolution Imaging Spectroradiometer (MODIS) land surface temperatures (LSTs) and validated by various ground-based datasets. The soil thermal properties of five soil types across the TP were estimated according to an empirical equation and in situ observed soil properties (moisture content and bulk density). The Temperature at the Top of Permafrost (TTOP) model was applied to simulate the

20   permafrost distribution. The results show that permafrost, seasonally frozen ground, and unfrozen ground covered areas of 1.06×10^6 km^2 (0.97-1.15×10^6 km^2, 90% confidence interval) (40%), 1.46×10^6 km^2 (56%), and 0.03×10^6 km^2 (1%), respectively, excluding glaciers and lakes. The ground-based observations of the permafrost distribution across the five investigated regions (IRs, located in the transition zones of the permafrost and seasonally frozen ground) and three highway transects (across the entire permafrost regions from north to south) have been used to validate the model. The

25   result of the validation shows that the kappa coefficient varies from 0.38 to 0.78 with an average of 0.57 at the five IRs and 0.62 to 0.74 with an average of 0.68 within the three transects. Compared with two maps compiled in 1996 and 2006 (kappa coefficients in average 0.06 and 0.35 in five IRs, 0.34 and 0.50 within three transects, respectively), the result of the TTOP modelling shows greater accuracy. Overall, the results provide much more detailed maps of the permafrost distribution and could be a promising basic data set for further research on permafrost on the Tibetan Plateau.

1 Introduction

As a main component of the cryosphere, permafrost is sensitive to climate changes (Wu et al., 2002b; Haeberli and Hohmann, 2008; Li et al., 2008; Gruber, 2012). Due to its unique and extremely high altitude with an average elevation over 4000 m (Qiu, 2008) and the lower mean annual air temperature (ranging from -9.7 to 6.8 ℃; Yang et al., 2010), the Tibetan Plateau (TP) (Zhang et al., 2002 and 2014) possesses the largest areas of permafrost in the mid- and low-latitude regions of the world (Zhao et al., 2004 and 2010). The presence of permafrost and its dynamics complicate the water and energy exchange between soil and atmosphere and thereby introduce greater uncertainty into Global Climate Models (GCMs) when predicting climate change (Romanovsky et al., 2002; Smith and Riseborough, 2002; Cheng and Wu, 2007; Riseborough et al., 2008; Zhao et al., 2010). To generate correct quantitative simulations, an accurate permafrost distribution of TP is evidently needed to improve the permafrost module description. Moreover, an accurate contemporary permafrost distribution map is of significant importance for serving as a standard to estimate permafrost degradation and as a basis for further quantitative research.

Over the past half-century, a significant amount of research has been conducted on the permafrost distribution of TP, and many permafrost maps (Shi and Mi, 1988; Li and Cheng, 1996; Brown et al., 1997 and 1998; Qiu et al., 2000; Wang et al., 2006) have been compiled to evaluate the distribution and thermal states of permafrost. These maps have been utilized widely to study the responses and feedback of permafrost to climate change (Ran et al., 2012). However, considerable differences in the permafrost areas and boundaries were found in these maps, from 1.12×10^6 to 1.50×10^6 km^2, due to different data collection periods, data sets, and methods (Yang et al., 2010; Ran et al., 2012). These maps represent different assessments of the permafrost distribution on the TP at different times.

In 1980s and 90s, permafrost maps were compiled by different scientists, and the permafrost boundaries were plot on topographic maps by hands with conventional cartographic techniques (Tong and Li, 1983; Shi and Mi, 1988; Li and Cheng, 1996). The representative and most widely used benchmark map is the *Map of Permafrost on the Qinghai-Tibetan Plateau* (Li and Cheng, 1996), and the permafrost boundaries were determined mainly based on air temperature isotherms combined with field data, satellite images and many relevant maps. After 2000, GIS techniques were applied to the permafrost mapping on the TP. Some simple empirical models with a minimal data requirement were established to consider the permafrost characteristics on the TP, such as the elevation model (Li and Cheng, 1999) and Mean Annual Ground Temperature (MAGT) (Nan et al., 2002). Meanwhile, some models with simplified physical processes applicable to high latitude permafrost were transferred to simulate the permafrost distribution on TP such as the frost index (Nelson and Outcalt, 1983) and the Temperature at the Top of Permafrost (TTOP) (Smith and Riseborough, 1996; Wu et al., 2002a). These models link permafrost temperature with surface temperature through seasonal surface transfer functions and subsurface thermal properties, which can provide reasonable assessments of permafrost distribution when the permafrost upper boundary conditions and regional soil thermal properties were satisfied. Recently, a global permafrost zonation index (PZI) was established based on the relationships between the air temperature and the occurrence of permafrost, which can represent broad spatial patterns but not provide actual permafrost extent (Gruber, 2012). Most

temperature fields that have previously been used in these models were also generated from spatially interpolated air temperature (Pang et al., 2011) or coarser resolution (e.g., 0.125°×0.125°) atmospheric reanalysis data (Gruber, 2012; Qin et al., 2015). Although air temperature produces inaccurate and excessively low resolution estimates of ground surface temperature (GST, defined as the surface or near-surface temperature of the ground (bedrock or surficial deposit) and measured in the uppermost centimeters of the ground), it was still widely used in the monitoring of permafrost in practical applications because of limited GST observations. In these studies, the N factor has been the optimal and effective way to transform the air temperature to the GST (Klene et al., 2001; Lunardini, 1978). With the recent development of infrared remote sensing technology, an increasing number of land surface temperature (LST, defined as the average temperature of an element of the exact surface of the Earth (e.g. surface of ground, vegetation canopy or snowcover) calculated from measured radiance; Gillespie., 2014) products derived from different satellite images have been applied to global and regional permafrost distribution research (Hachem et al., 2009; Kääb, 2008; Langer et al., 2010; Nguyen et al., 2009; Westermann et al., 2012 and 2015). These products were used as effective alternatives for GST, especially for in-situ observation limited regions, such as the TP (Zhang et al., 2004). However, the LSTs observed by satellite sensors are instantaneous values at passing times and must be transformed into mean daily temperature to serve as the thermal state of each day before being utilized. Wang et al. (2011) averaged the twice-daily LST observations of the Moderate Resolution Imaging Spectroradiometer (MODIS) sensors on board Terra satellite to drive the TTOP model, and their results show that there was a systematic bias with the ground observations because of different observation times (Wang et al., 2011). In addition, the limited available soil thermal property spatial datasets create another problem when modelling permafrost distribution. Most previous soil surveys were carried out in seasonally frozen ground or permafrost along the Qinghai–Tibet Highway (Li et al., 2014; Li et al., 2015a) rather than permafrost regions in the plateau hinterland due to the harsh climate and inconvenient access. Therefore, soil thermal properties have generally been estimated via soil types generated from a limited number of plateau geologic classification studies (Li et al., 2015b; Wang et al., 2011). Overall, there are insufficient field investigations to take part in the modelling and validate the maps and their accuracy.

Recently, field survey datasets have been obtained based on the project "Investigation of Permafrost and Its Environment over The Qinghai–Xizang(Tibet) Plateau" conducted by the Cryosphere Research Station on Qinghai–Xizang Plateau, Chinese Academy of Sciences (CAS), which could provide validation data of permafrost distribution maps. In addition, some new progress in research on remote sensing LST applications and spatial soil characteristics on the TP were studied. An empirical model of daily mean LST was established and performed well in continuous permafrost regions of the Central TP (Zou et al., 2014). Li et al. (2015b) studied the relationships between environmental factors and soil types in the permafrost region on TP, and they utilized a decision-making tree to spatialize the soil types. The results exhibited good reliability and could be used to realize the spatialization of soil thermal properties.

This study aims to generate a new permafrost distribution map on the TP with remote sensing LST products and the investigated soil thermal properties, and to validate the accuracy of the results in this study and the two most widely used permafrost maps. In this study, a multiple linear regression model based on MODIS LST was established, and ground-

100   based LST observations were employed to calibrate the results. Soil thermal conductivities of each soil type on the TP were calculated via in situ observed soil moisture content and bulk density. TTOP model was employed to simulate the permafrost distribution, and the results were validated by the observed permafrost distributions of boreholes, five investigated regions (IRs, located in the transition zones of the permafrost and seasonally frozen ground) and three transects (across the entire permafrost regions from north to south). The TTOP modelling result was also compared with

105   that of two recent benchmark maps (made in 1996 and 2006).

2 Materials and methods

2.1 Field survey datasets

The comprehensive investigation of permafrost and its environments on the TP was conducted from 2009 to 2014. Five investigated regions (IRs)—WenQuan (WQ) (Zhang et al., 2011 and 2012) and Budongquan-Qingshuihe (B-Q) in the

110   Eastern TP, AErJin (AEJ) in the Northeastern TP, GaiZe (GZ) (Chen et al., 2016) in the Southern TP, and XiKunLun (XKL) (Li et al., 2012) in the Western TP (Fig.1), which are located in the transition zones between permafrost and seasonally frozen ground with different climatic and geographic conditions—were selected for detailed investigation. Ground-based observations, mechanical excavation, geophysical exploration (Ground Penetrating Radar, GPR; Time-domain ElectroMagnetic, TEM), and borehole drilling were employed, and comprehensive surveys of the permafrost

115   distribution boundary, soil, vegetation, climate, and landform were carried out in all five IRs. The datasets of ground temperature profiles, spatial distribution of vegetation (Wang et al., 2016) and soil types (Li et al., 2014 and 2015a) were obtained and a long-term permafrost monitoring network was established, including automatic weather station and borehole records.

2.1.1 Boreholes and soil pits

120   Field survey datasets including ground temperature, soil moisture content, and bulk density were obtained in the investigation. The ground temperature, measured by temperature probes at different depths (generally set at 0.5 m intervals from 0 to 5 m, 1 m from 5 to 20 m, 2 m from 20 to 40 m, 5 m from 40 to 60 m, and 10 m greater than 60 m) in boreholes were used to determine whether permafrost exists. The soil samples were collected according to depth increments at each pit. The field bulk density (weight of the soil per unit volume) was measured by the clod method.

125   Samples for moisture determination were stored in aluminium sampling boxes and carefully sealed to prevent changes of soil moisture. The soil moisture content was expressed by weight as the ratio of the mass of water present to the dry weight of the soil sample (Wu et al., 2016). Considering that the sampling period was concentrated from July to October, the weighted average moisture content by depth was used to denote the mean state of each pit. The soil moisture content and bulk density were used to calculate the soil thermal conductivity. The statistics of the field survey samples show a

130   total of 125 boreholes and 199 soil pits in five IRs (Table 1).

2.1.2 Permafrost maps of five investigated regions

The permafrost maps of five IRs were used as the validation data in this study. In the local region, the elevation and terrain factors have greater influence on permafrost occurrence than that of longitude and latitude, especially on mountainous permafrost (Riseborough et al., 2008). The lower limit of permafrost (LLP) was determined based on the linear regression relationship between MAGT and elevation of boreholes, and the elevation where MAGT equals to 0 ℃ was regarded as the LLP (Li et al., 2012; Zhang et al., 2012; Chen et al., 2016). In view of the influence of aspects on LLPs, the boreholes were classified into three types: north-facing, south-facing and east-west facing and the LLP of each type was determined respectively; then, the permafrost distribution was generated based on the LLPs of different aspects and the digital elevation model (DEM) data, and a portion of the observed results of boreholes and geophysical methods (GPR and TEM) was reserved to validate the maps (Li et al., 2012; Zhang et al., 2012). For example, the results of GZ IR showed that the LLP was about 4950 m for north-facing, 5000m for east-west-facing, and 5100 m for south-facing slopes (Chen et al., 2016).

2.1.3 Permafrost distribution of three highway transects

The three highway transects were set as follows (Fig.1): National Highway 214 (Qinghai–Yunnan Highway, hereafter G214) from Northern Ela Mountain to Qingshuihe Town, National Highway 109 (Qinghai–Xizang Highway, hereafter G109) from Xidatan to Nagqu, and National Highway 219 (Xinjiang–Xizang Highway, hereafter G219) from Kudi to Shiquanhe Town; the overall transect lengths of G214, G109 and G219 were approximately 400, 750 and 900 km, respectively. Three transects across the entire permafrost regions from north to south in the Eastern, Central and Western TP were established. Many permafrost geological conditions were obtained in the process of the construction and renovation of three highways, and many permafrost roadbed monitoring sections were subsequently set along the highways (Jin et al., 2008; Sheng et al., 2015). Based on these background data and our investigated results (geophysical and drilling exploration), the permafrost distribution limits and geothermal features of three transects were generated and used as the validation datasets.

2.2 Spatial datasets

2.2.1 Existing two benchmark permafrost maps

The most widely used permafrost distribution benchmark maps are 1) The *Map of Permafrost on the Qinghai–Tibetan Plateau*, which was compiled by Lanzhou Institute of Glaciology and Geocryology, Chinese Academy of Sciences (hereafter TP-1996) to support basic research on cryospheric dynamics in China (Li and Cheng, 1996). TP-1996 synthesizes field data, literature, aerial photographs, satellite images and many relevant maps and shows that the area of permafrost is 1.41×10^6 km^2. 2) The *Map of the Glaciers, Frozen Ground and Deserts in China* was compiled by Cold and Arid Regions Environmental and Engineering Research Institute, Chinese Academy of Sciences (hereafter TP-2006) (Wang et al, 2006). In this map, the permafrost distribution was generated using a 0.5 °C MAGT isotherm as a threshold, which shows that the area of permafrost is 1.12×10^6 km^2. The MAGT was interpolated based on the relationship between elevation/latitude and the MAGT observation from all 76 boreholes along the Qinghai–Xizang Highway (Nan et al,

165   2002).

2.2.2 MODIS LST products

The MODIS LST data used in this study were the 1 km gridded clear-sky MOD11A2 (Terra MODIS) and MYD11A2 (Aqua MODIS) products (reprocessing version 5), which span from 2003 to 2012. The results of the radiance-based and temperature-based validation indicated that the accuracy of the global MODIS LST product is better than 1 ℃ in most

170   cases, including lakes, homogeneous vegetation and soils under clear-sky conditions (Wan et al., 2002 and 2004; Coll et al., 2005; Wan and Li., 2008; Wan., 2008). Langer et al. (2010) and Westermann et al. (2011) focused on weekly averages and demonstrated an agreement generally better than 2 ℃ for MODIS LST for the summer season, at permafrost sites in Siberia and Svalbard, respectively.

Both MOD11A2 and MYD11A2 provide two observations (daytime and nighttime), which means that there are four

175   LST observations for the same pixel per day. The temporal resolution of MOD11A2/MYD11A2 was 8 days, the LST values represent the 8-day average LST values (the missing values were ignored in the calculation) (Wan, 2009; Wan and Dozier, 1996), and there are theoretically 46 groups of LST values every year. While the 8-day MODIS LST products have more reliable data than daily products, they still have numerous missing values when establishing the mean daily LST empirical models due to clouds or other factors (Prince et al., 1998). In this study, the Harmonic Analysis Time-

180   Series (HANTS) algorithm (http://gdsc.nlr.nl/gdsc/en/tools/hants), which was developed to deal with time series of irregularly spaced observations and to identify and fill the missing values (Roerink et al., 2000), was applied for smoothing and reconstructing MODIS LST series on a per-pixel basis for the entire study area. The parameters set for the HANTS analysis was described in detail in Xu et al. (2013).

The full coverage of the whole TP needs total 13 swathes (h23v04, h23v05, h24v04, h24v05, h24v06, h25v04, h25v05,

185   h25v06, h26v04, h26v05, h26v06, h27v05 and h27v06) of MOD11A2/MYD11A2 products. The Terra overpass time is around 10:30 AM (local time) in its descending mode and 10:30 PM in its ascending mode. The Aqua overpass time is around 1:30 PM in its ascending mode and 1:30 AM in its descending mode (https://modis.gsfc.nasa.gov/). The MODIS LSTs represent instantaneous observation values, and the overpass times of the satellites do not accurately correspond to standard meteorological observation times (Beijing time: 2:00, 8:00, 14:00, and 20:00) (China Meteorological

190   Administration, 2003). Therefore, an arithmetic average of the four LST observations with the same weights will produce a large deviation from the mean daily LST (Wang et al., 2011). In this study, a multiple linear regression was employed to distribute different weights to each MODIS LST observation to establish the mean daily LST empirical model. The details of processing were described in the reference Zou et al. (2014), and the model validation in three permafrost sites showed that the determination, mean error, mean absolute error and root mean squared error of mean daily LST was 0.91

195   to 0.93, -0.21 to 1 ℃, 2.28 to 2.42 ℃ and 2.96 to 3.05 ℃, respectively. In this study, the empirical formula is as follows:

$$LST_{daily} = 0.18 \times Terra_{day} + 0.269 \times Terra_{night} + 0.143 \times Aqua_{day} + 0.435 \times Aqua_{night} + 0.896 \tag{1}$$

where LST_{daily} is the mean daily LST, $Terra_{day}$ is daytime LST observation of MOD11A2, $Terra_{night}$ is nighttime LST observation of MOD11A2, $Aqua_{day}$ is daytime LST observation of MYD11A2, and $Aqua_{night}$ is nighttime LST observation of MYD11A2.

200   The calculations of the thawing indices (Thawing Degree Days, TDD) and freezing indices (Freezing Degree Days, FDD) were based on the 8-day average LST calculated from the previous processing. The procedures were realized using the IDL programming language, and the FDD and TDD from 2003 to 2012 were obtained and averaged as the model inputs.

2.2.3 Soil thermal properties

Soil thermal characteristics were modeled according to parameters measured from soil types encountered in the field.
205   The classification of soil types was performed using the Decision Tree See 5.0 software and the Soil-Land Inference Model (SoLIM) in conjunction with soil type and environment factor data (Li et al., 2014; Li et al., 2015b). According to the Soil Taxonomy System, there are five soil orders on the TP as follows: Gelisols, Aridisols, Mollisols, Inceptisols, and Entisols. Considering the availability of soil sample parameters, the characteristics of sampling regions, and model applicability, the empirical model of soil thermal conductivity proposed by Kersten (1949) was adopted in this study.
210   The equation of thawed soil thermal conductivity is

$$k_t \ = \ 0.1442 \times (0.7 \times log\omega + 0.4) \times 10^{(0.6243 \times \gamma_d)} \tag{2}$$

Furthermore, the equation of frozen soil thermal conductivity is

$$k_f \ = \ 0.01096 \times 10^{(0.8116 \times \gamma_d)} + 0.00461 \times 10^{(0.9115 \times \gamma_d)} \times \omega \tag{3}$$

where k_t/k_f is the thermal conductivity (W m^{-1} K^{-1}) of thawed/frozen soil, ω is the soil moisture content (%), and γ_d is
215   the soil bulk density (kg m^{-3}). Both ω and γ_d were measured via soil samples collected in the field survey. The soil samples were classified according to soil orders; moisture content and bulk density values were averaged within soil orders to eliminate abnormal values (Table 2, the values show the mean with standard deviation of soil thermal parameters of each type).

2.2.4 Glacier and lake data

220   The spatial distribution and area of glacier and lake data on the TP were from the Second Glacier Inventory Dataset of China (Guo et al., 2014) and the Cryosphere Information System (Li, 1998) provided by Cold and Arid Regions Science Data Center (http://westdc.westgis.ac.cn).

2.3 TTOP model

Considering the model's usefulness and sophistication, spatial scales and available datasets (Riseborough et al., 2008), we selected the Temperature at the Top Of Permafrost (TTOP) model (Smith and Riseborough, 1996) to simulate the permafrost distribution on the TP.

The TTOP model can be expressed as follows:

$$TTOP = \frac{k_t/k_f \times TDD - FDD}{P} = \frac{(r_k \times n_t \times I_t) - (n_f \times I_f)}{P} \qquad (4)$$

where P is the annual period (365 days). TDD ($n_t \times I_t$) is the ground surface thawing indices, and FDD ($n_f \times I_f$) is the ground surface freezing indices. n_t and n_f are n factors of the thawing and freezing seasons, and I_t and I_f are the air temperature thawing and freezing indices, respectively. $r_k = k_t/k_f$ is defined as the ratio of the thermal conductivity coefficient when soil is thawing and freezing. In this study, the modified MODIS LST data processed in *Section 2.2.2* was used as GST to derive the TDD and FDD, and the r_k is calculated from the soil properties derived from process in *Section 2.2.3*.

From Equation 4, if the *FDD* is greater than $TDD \times k_t/k_f$ ($n_f \times I_f > r_k \times n_t \times I_t$), *TTOP* will be below 0 °C, and permafrost exists. This processing was realized in the ArcGIS software program with the following expression:

$$D = \begin{cases} 1, & TTOP \leq 0 \qquad permafrost \\ 0, & TTOP > 0 \qquad seasonally\ frozen\ ground \end{cases} \qquad (5)$$

The regions of glacier and lake were excluded from the permafrost distribution modelling of the TTOP model. In addition to permafrost and seasonally frozen ground, unfrozen ground was also identified in this study. The unfrozen ground was defined as the region where the extreme minimum LST ≥ 0 °C. The night Aqua MODIS LST (observation time approximately 3:00 a.m.) was employed as input data for the determination of unfrozen ground area. The uncertainty analysis of total permafrost area was conducted in R statistical software (version 3.3.1, www.r-project.org) using the Percentile Method, and we use a 90% confidence interval to find the range of total permafrost areas. The modelling scheme in this study is shown in Fig.2.

2.4 Accuracy evaluation

The permafrost distribution of the borehole locations, five IRs and three transects were employed to estimate the accuracies of the three maps (TP-1996, TP-2006 and TP-2016). First, the spatial distribution of borehole temperature data across a permafrost domain or seasonally frozen ground area has been used as the criterion of advantages and disadvantages of results for three time snapshots of 1996, 2006 and 2016. The permafrost distribution across the five IRs and three transects were selected as the real values to validate the three maps.

To evaluate the agreement of the simulated permafrost distribution and the observed results, the kappa coefficient (K) (Cohen, 1960), which measures the degree of agreement, was selected for accuracy evaluation.

$$K = \frac{s/n - (a_1b_1 + a_0b_0)/n^2}{1 - (a_1b_1 + a_0b_0)/n^2} \tag{6}$$

where the total number of pixels is n, and s is the number of pixels in which the simulation and investigated results agree. The number of investigated result pixels with permafrost is a_1, and those without are a_0, and the simulated map pixel numbers are b_1 and b_0. Empirically and statistically arbitrary quality values for K have been proposed; e.g., Cohen (1960) suggested that $K \geq 0.8$ signifies excellent agreement, $0.6 \leq K < 0.8$ represents substantial agreement, $0.4 \leq K < 0.6$ represents moderate agreement, $0.2 \leq K < 0.4$ represents fair agreement, and a lack of agreement corresponds to $K < 0.2$.

3 Results

3.1 Permafrost distribution modelling of TTOP

Fig.3 shows the simulated permafrost distribution of the TTOP model on TP (TP-2016). The distribution areas of permafrost and seasonally frozen ground were 1.06×10^6 km^2 with 90% confidence interval of 0.97 - 1.15×10^6 km^2, and 1.46×10^6 km^2, excluding glaciers and lakes, which account for 40% and 56% of the total TP area, respectively. The result shows that the permafrost distribution was centred in Southern Qinghai and Northern Tibet. The Northern Qiangtang Plateau and Kunlun Mountain were the regions with the most permafrost developed regions which extends west and northwest to Karakoram Mountain. The permafrost continuity decreases gradually as the elevation decreases and the ground temperature increases with increasing distance from the central region. The geographic north and south boundary of permafrost were Xidatan and Anduo from the mark sites of Qinghai–Xizang Highway. There were a few areas of permafrost in the high mountains from Anduo to the Southern Tibet Valley. Due to the existence of the Bayan Har Mountains and Anemaqen Mountain, whose elevations are above 5000 m, there are permafrost occurrence in the Eastern TP. Some unfrozen ground exists in the southeast margin of the TP, whose area is approximately 0.03×10^6 km^2 (account for 1% of the total TP area).

3.2 Validation with borehole observations

The boreholes can determine whether permafrost exists or not. Fig.4 shows the spatial distribution of borehole locations at permafrost or seasonally frozen ground in five IRs of three maps. Different combinations were set up to analyse the difference of the three results; columns a, b, and c show the results of TP-1996, TP-2006, and TP-2016, and rows 1, 2, 3, 4, and 5 show the results of XKL, GZ, AEJ, B-Q, and WQ IRs, respectively. The result shows that TP-1996 is insensitive to the geographical boundaries across all five IRs, and there are plenty of erroneous interpretations of both permafrost and seasonally frozen ground. TP-2006 has higher sensitivity to the boundaries, especially in WQ IR; however the recognition of the other four IRs is not good enough, and the areas of permafrost distribution are overestimated. Compared to TP-1996 and TP-2006, TP-2016 performed better at identifying the geographic boundary of permafrost distribution, identifying almost all the boundaries of the five IRs correctly, especially for the seasonally

frozen ground in the valley of the Northwestern XKL IR (Fig.4 c1) and that around the lakes of the Eastern AEJ IR (Fig.4 c3). TP-2016 featured some misjudgment, mainly affected by local terrain factors including the seasonally frozen ground distributed in valleys and a few permafrost spots at the margin, such as the two seasonally frozen ground boreholes in the Northern AEJ IR (Fig.4 c3) and three permafrost boreholes at the southwestern limit of GZ IR (Fig.4 c2).

3.3 Validation with five investigated regions (IRs)

The permafrost distributions of five IRs were employed as truth values to validate the modelling results of three maps to analyse their performance in terms of geographical boundary recognition ability. TP-1996 performed worst at recognizing the boundaries of permafrost in five IRs; it misidentified all boundaries, with a low kappa coefficient (K < 0.2), due to more misjudgment or overestimated permafrost pixels. TP-2006 also performed poorly in the XKL, GZ, and AEJ IRs (K < 0.2) but performed better in the B-Q and WQ IRs, with a kappa coefficient reaching 0.63 and 0.77. TP-2016 had poor performance in the AEJ IR; the kappa coefficient reached only 0.38, which is an improvement to some extent over that of the former two. In addition, it represents moderate agreement with the XKL and GZ IRs and substantial agreement with the B-Q and WQ IRs, whose kappa coefficients were 0.54, 0.48, 0.68 and 0.78, respectively. The average accuracies of TP-1996, TP-2006 and TP-2016 were 0.06, 0.35 and 0.57, respectively. TP-2016 performed best in the validation with the investigated permafrost distribution from both the individual and averaged accuracies of five IRs (Table 3). Moreover, the TP-2016 perform better to identify the permafrost boundary in the regions with complex terrain because of sharp changes in LST within short distances, such as the WQ, B-Q and XKL IR. For GZ and AEJ IRs, where surface relief are much low, the TP-2016 performs not as good as the other three IRs. In addition, the worst performance in AEJ IR might also due to none soil pits in the investigation and the soil thermal properties inferred completely from the relationship between the environmental factors and the soil samples of the other four IRs.

The results of the AEJ IR and surrounding area are selected to compare the differences among the three maps (Fig.5). In the AEJ IR, the investigated result shows that the seasonally frozen ground is mainly distributed at the northern valley and the Eastern Ayakekumu Lake surrounding areas and features permafrost. TP-2006 shows all judgement for permafrost in the AEJ IR, which obviously overestimated the area of permafrost. Although TP-1996 shows some seasonally frozen ground in the Northwestern AEJ IR, the locations were misjudged. TP-2016 judged approximately 30% seasonally frozen ground in the Northern and Eastern AEJ IR. Although the correct pixels were few, the locations in the eastern part were just at the geographic boundary of permafrost. The observed MAGT of the borehole closest to Ayakekumu Lake was 3 °C, which means that seasonally frozen ground exists there, and TP-2016 accurately modelled this phenomenon. In the regions around the AEJ IR, TP-2016 simulated the seasonally frozen ground around Aqikekule Lake (area approximately 350 km^2) and its supply river, and this did not appear in the other two maps. Most lakes on TP are formed due to tectogenesis; the major axis basically remains consistent with the main structure directions and the secondary level fracture direction, and there generally exists penetrative or nonpenerative taliks under and around tectonic lakes (Zhou et al., 2000). TP-2016 also shows seasonally frozen ground in the mountainous region proximate

to the Pitileke River, while the other two maps did not identify that. TP-2016 was more accurate in this respect; the ground temperature was affected by the higher temperatures of the water bodies, resulting in the appearance of seasonally frozen ground.

The permafrost distribution of TP-1996 and TP-2006 was modelled according to the relationship between temperature and three-dimensional zonalities (longitude, latitude, and elevation) (Cheng, 1984). The higher weight of elevation from the regression equation determined that it has greater influence than that of longitude and latitude when interpolating temperature (air temperature or MAGT). The high continuity and low variability of the elevation difference in permafrost regions lead the results to appear more continuous; however, the temperature differences caused by local factors (e.g., lakes or rivers) are masked to a large degree and thus result in an excessive occurrence of the lower extrapolated temperature; this could be used to explain the overestimated area of permafrost distribution in the previous TP-1996 and TP-2006. The application of the remote sensing data can better reveal the spatial heterogeneity of LST. Relative to the two benchmark maps, the result of TP-2016 driven by the processed MODIS LST in this paper is very sensitive to seasonally frozen ground formed by surface water, and the results show that there are many seasonally frozen ground surrounding lakes and major rivers that corresponding to the previous studies (Lin et al., 2011; Niu et al., 2011).

3.4 Validation with three transects

The permafrost distribution of three transects (G214, G109 and G219) of three maps were extracted to compare to the investigated results to comprehensively evaluate their performance on the mainly permafrost developed regions on the TP. The accuracy statistics of three maps in the three transects are listed in Table 4. TP-1996 has the worst accuracy in the three maps with an average kappa coefficient of 0.34. The accuracy of TP-2006 is higher than that of TP-1996 with an average kappa coefficient of 0.50; it performed well especially in transect G109. TP-2016 has the highest accuracy; the kappa coefficients are 0.62, 0.69, and 0.74 for G214, G109, and G219, respectively, with an average of 0.68. TP-2016 performed best in the validation with the investigated permafrost distribution from both the individual and averaged accuracies of the three transects. In the three transects across all permafrost regions from north to south in the Eastern, Central and Western TP, which include most permafrost distribution characteristics in TP, the validation results should be a synthetic evaluation of the three maps.

Fig.6 shows the distributions of permafrost and seasonally frozen ground along the G109 transect of the three maps and investigated result; the elevation and mark sites were also added for analysis. To conveniently compare, the G109 transect was divided into five segments according to the investigated result as follows: two continuous permafrost regions (from XDT to Southern FHSYK, and Southern YSP to Northern AD), one region of seasonally frozen ground only (from Southern LDH to NQ) and two regions in which permafrost and seasonally frozen ground coexist (from WL to YSP, and AD to LDH). The comparison shows that the three maps performed well in two continuous permafrost regions; almost all permafrost is identified correctly except for several seasonally frozen ground areas in CMEH and BLH of TP-1996. In the region of seasonally frozen ground only, TP-1996 judged permafrost from AD to NQ, which is different from the investigated result and overestimated the permafrost area in this region. TP-2006 and TP-2016 identified that only

seasonally frozen ground exists in this region, which is highly consistent with the investigated result. In two regions where permafrost and seasonally frozen ground coexist, a large difference occurred between the three maps and the investigated result. TP-2006 shows that continuous permafrost exists from XDT to Northern AD, performing poorly in the recognition of the seasonally frozen ground, and thus overestimating the area of permafrost in the G109 transect. TP-1996 performed better than TP-2006, which recognized some of the seasonally frozen ground in TTH, TTH', YSP and AD; however, the widths and locations reveal bias from that of the investigated result. TP-2016 identified almost all locations of seasonally frozen ground correctly with smaller width difference, which is more consistent with the investigated result than the former two. It is worth mentioning that both TP-2006 and TP-2016 identified the sporadic permafrost in LDH, which was generally expected as the southern limit of permafrost in previous studies.

In the G109 transect, seasonally frozen ground mainly exist due to the surface water effects, regional geologic structure/geothermal effects and penetration/radiation effects, which cause a discontinuity in the plane and depth of continuous distribution of permafrost (Zhou et al., 2000). Due to the large streamflow and high water temperature of TTH, TTH' and Buqu (flow through YSP) rivers, the penetrative taliks not only developed on the riverbed and high floodplain, but also expanded to the first or second terrace (width generally reached 5–10 km). Additionally, bare land, gravel layer exists, and a higher mean annual air temperature was beneficial to precipitation infiltration, which created active thermal transfer conditions; therefore, the seasonally frozen ground exist in TTH and YSP were also affected by penetration/radiation effects. However, for the rivers with less streamflow and higher latitude, such as the CMEH and BHL rivers, the nonpenetrative taliks are much smaller (generally < 100 m) and thus almost impossible to identify. The seasonally frozen ground in Northern WL were mainly affected by regional geologic structure/geothermal effects, which has been validated by the results of engineering geologic surveys of the Qinghai–Xizang Highway and Railway (Jin et al., 2008). From the kappa coefficients of the three maps and investigated result (Table 4) along the G109 transect, TP-2016 can better identify the seasonally frozen ground of several kilometres in width caused by local factors (surface water, geothermal, and permeate/radiation effects).

3.5 Spatial difference among the three maps

The kappa coefficients of each pair among the three maps were calculated (Table 5) to analyse the spatial difference. TP-1996 revealed low consistency with both TP-2006 and TP-2016; the kappa coefficients were 0.56 and 0.53, respectively, which indicates a large difference. TP-2006 has a substantial agreement with TP-2016; the kappa coefficient reached 0.71. The spatial difference between each pair among the three maps were compared (Fig.7). Compared with TP-2006 and TP-2016, TP-1996 overestimated the permafrost area, which was mainly distributed at the Southeastern TP, south margin of continuous permafrost, and predominantly continuous and island permafrost in the Southern TP. In addition, TP-1996 misjudged some seasonally frozen ground on the continuous permafrost edge and the interior TP. The permafrost distribution area of TP-2006 was close to that of TP-2016; the difference mainly exists at the regions of interior TP, south margin of continuous permafrost, and surrounding regions of the Bayan Har Mountains and Eastern Nyainqntanglha Mountains.

4 Discussion

385   TTOP was formulated with the modified MODIS LST, rather than ground surface temperature (GST) in this study. It is well known that MODIS LST observes a mixture of the vegetation canopy, snow cover, and ground surface, depending on the region and seasons. The snow cover and vegetation might play significant influences on the relationship between the GST and MODIS LST, depending on the snow depth and duration (Zhang, 2005), vegetation height and coverage. The snow cover distribution is spatially quite variable over the TP (Fig.8 a), with the most persistently snow-covered

390   areas occurring in the southeastern and western edge of the TP and some alpine regions with the elevation higher than 6000 m (Qin et al., 2006; Pu et al., 2007). Overall, the snow cover is rare, thin (< 3 cm) and has a short duration (mostly existed less than one day for a single snow event) due to the strong solar radiation and wind in the vast interior and the northern TP (Che et al., 2008; Huang et al., 2017), where the permafrost most developed. Therefore, although the thin snow cover might have a cooling effect on GST due to the high albedo of fresh snow and a rapid process of snowmelt

395   (Zhang, 2005), the cooling effect may be very short and have very little effect in our study due to the very short duration. For the vegetation types of the permafrost region on the TP (Fig.8 b), the alpine ecosystem in permafrost region and its vicinity are all composed of grassland, characterized by dwarf and sparse plants (Wang et al., 2016). The vegetation coverage in most of the permafrost region was less than 30% (Lehnert et al., 2015), and even less than 10% in the middle and western TP. In view of the condition of both snow cover and vegetation on the TP, there are only slight differences

400   between GST and MODIS LST in average, and even much small in FDD and TDD in our study area. In addition, the HANTS algorithm might caused some bias under the cloudy sky condition, and therefore, further evaluation of the algorithm was not performed in this study because it has been proved to be an effective approach for filling the gap of MODIS LST data on the TP where clear-sky conditions dominated (Xu et al., 2013).

    The dataset used in the earliest maps (compiled in 1980s and 90s) including air temperature, field data, aerial photographs,

405   satellite images and many relevant maps (Tong and Li, 1983; Shi and Mi, 1988; Li and Cheng, 1996). The permafrost boundary was mainly based on a threshold of air temperature isotherm, and modified in several regions (such as Qinghai–Xizang Highway, Qinghai–Yunnan Highway and Hengduan mountains) with field data by the authors' knowledges. The threshold was determined by the empirical statistical relationship between permafrost occurrence and meteorological observations in the Eastern TP (Li and Cheng, 1996), while the universality of the threshold is questionable in the western

410   TP due to insufficient data. In addition, high uncertainty exists in the air temperature interpolation because of the scarcity, unevenly distributed (more in the Eastern TP and less in the Western TP; more in lower elevation and less in higher elevation; very few in permafrost region) monitoring sites, resulting in the low accuracy of extrapolated air temperature of the TP (Lin et al., 2002; Li et al., 2003), especially for the permafrost region. Moreover, the permafrost maps were compiled with conventional cartographic techniques that plotted the permafrost boundaries on the topographic maps by

415   hand (Tong and Li, 1983; Shi and Mi, 1988; Li and Cheng, 1996), the artificial error was very difficult to control, depending on the mapper's knowledge and skill. The above mentioned factors leaded to high uncertainties in these maps. Actually, these maps are much emphasized on a broad concept of the possible permafrost regions, which overestimated the permafrost areas too much (Wang et al., 2016). The permafrost mapping of TP-2006 was based on the MAGT that

in consideration of the characteristics of high altitude permafrost. The regional MAGT was interpolated based on the relationship between elevation/latitude and the borehole observations along the Qinghai–Xizang Highway (Nan et al, 2002). The MAGT model performed better in the Central TP than that in the Eastern and Western TP, which has been demonstrated in the validation of the three transects. In view of the medium spatiotemporal resolution and sensitivity to spatial temperature heterogeneity of MODIS LST data used in the mapping of TP-2016, it can represent accurately the spatial pattern of LST on the TP. In addition, the MODIS LST data was calibrated by the ground-based LST observations obtained from automatic weather stations in typical permafrost regions (Zou et al., 2014), which is corresponding to actual climate condition of permafrost region. Moreover, the subsurface thermal properties derived from soil investigation data were also considered in the TTOP model. The improvement of upper boundary conditions of the permafrost model and the use of large quantities of reliable in situ observed datasets, leads to a high modelling accuracy.

In the earliest maps, only some observed data from the field sites along Qinghai–Xizang Highway were used for map evaluation (Tong and Li, 1983; Shi and Mi, 1988; Li and Cheng, 1996). For TP-2006, the threshold of 0.5 °C MAGT was determined by the sensitivity analysis of comparison with the TP-1996, without independent validation (Nan et al, 2002). The validation in this study showed that the accuracy of TP-2006 was higher than that of TP-1996; however, it highlights the excessive elevation effects when interpolating the MAGT and masks the effects of local factors to some degree. Additionally, the better performance of TP-2006 in the B-Q and WQ IRs might be explained by the similar geomorphology to Qinghai–Xizang Highway, because these two IRs were closer to the highway relative to the other three IRs. This suggests that the MAGT model could reflect the permafrost distribution when there is sufficient borehole ground temperature observations, and that is why we use it to modelling the permafrost distribution of five IRs. The validation results of the five IRs emphasized on the performance on recognizing permafrost boundaries and that of the three transects emphasized the overall evaluation of the three maps. Overall, the validation results of both the five IRs and three transects suggested that TP-2016 performed the best and achieved the highest accuracy among the three maps. The results provide a standard permafrost distribution map on the TP in contemporary climate. It is worth mentioning that the approach in this study is useful for mapping purposes, but it should not be used for modelling transient responses of permafrost to climate change which should use one-dimensional numerical models (e.g. NEST, GIPL model, or T-ONE).

The ground temperatures of permafrost on the TP were increasing during the past several decades (Wu and Liu, 2004; Wu and Zhang, 2008; Zhao et al., 2010), which means disequilibrium of permafrost under climate warming, and thereby any map based on a contemporary climate forcing likely underestimates permafrost extent. However, there exists a long response time of permafrost bodies to atmospheric conditions (Riseborough, 2007; Romanovsky et al., 2010; Smith et al., 2010). The increasing rates of ground temperatures were much lower in the TP than that in the circumpolar regions, and even much lower for the warm permafrost (Wu and Zhang, 2008; Smith et al., 2005; Zhao et al., 2010), which is mostly distributed near the permafrost boundaries. Moreover, the degradation of permafrost in these regions was characterized by deepening of active layer, rather than the disappearance of permafrost. It was said that the changes of the permafrost distribution on the TP might be very limited in the past several decades. Therefore, the spatial difference

among the three maps might be mainly induced by the differences in methods and data sources. The TP-2016 could be
455   used as the bench mark map for permafrost distribution on the TP, although more works is needed to improve the accuracy of surface forcing and the soil parameters.

5 Conclusions

This study exploits the advantages of the medium spatiotemporal resolution of MODIS LST products to construct a database of mean daily LST of the TP. The permafrost distribution is simulated by the TTOP model combined with
460   ground observation and soil investigated datasets, and the model was validated against the permafrost distribution obtained from the borehole temperature data, five IRs and three transects and compared to two recent benchmark maps. From the validation with borehole temperature data, the suggested method of permafrost boundary identification shows a better result than the two maps, especially for the seasonally frozen ground in valleys and around lakes. The accuracy of method validation shows that the TP-2016 case has the highest kappa coefficients for both five IRs and three transects.
465   The average coefficients are 0.57 and 0.68, respectively. The modelling estimation shows that 1.06×10^6 km^2 of permafrost (0.97×10^6 km^2-1.15×10^6 km^2, 90% confidence interval), 1.46×10^6 km^2 of seasonally frozen ground, and 0.03×10^6 km^2 of unfrozen ground could be on the TP. Compared with two recent benchmark maps, the TTOP model is superior in recognizing the boundary of permafrost, especially in the areas surrounding lakes and rivers. The new permafrost distribution map represents a promising basic dataset for further permafrost research.

470   **Acknowledgements.** We thank the Atmosphere Archive and Distribution System for providing MODIS land products, and Cold and Arid Regions Science Data Center for data of glacier, lake and snow depth on the Tibetan Plateau. This research was financial supported by the National Major Scientific Project of China "Cryospheric Change and Impacts Research" (2013CBA01803), the Creative Research Groups of National Natural Science Foundation of China (No. 41421061), the key project of the Chinese Academy of Sciences (KJZD-EW-G03-02). We would also gratefully
475   acknowledge Professor Jerry Brown, Stephan Gruber and Sergey Marchenko for their helpful and constructive suggestion on the manuscript.

References

Brown, J., Ferrians Jr, O. J., Heginbottom, J. A., and Melnikov, E. S.: Circum-Arctic Map of Permafrost and Ground-Ice Conditions. Circum-Pacific Map Series CP-45, scale 1:10,000,000, 1 sheet. US Geological Survey in Cooperation with the Circum-Pacific Council for Energy and Mineral Resources: Washington, DC, 1997.

Brown, J., Ferrians Jr, O. J., Heginbottom, J. A., and Melnikov, E. S.: Circum-Arctic Map of Permafrost and Ground Ice Conditions. Digital media. National Snow and Ice Data Center/World Data Center for Glaciology: Boulder, CO, 1998.

Che, T., Xin, L., Jin, R., Armstrong, R., and Zhang, T.: Snow depth derived from passive microwave remote-sensing data in China, Ann. Glaciol., 49(1), 145-154, 2008.

Chen, J., Zhao, L., Sheng, Y., Li, J., Wu, X. D., Du, E. J., Liu, G. Y., and Pang, Q. Q.: Some Characteristics of Permafrost and Its Distribution in the Gaize Area on the Qinghai-Tibet Plateau, China, Arct. Antarct. Alp. Res., 48(2), 395-409, 2016.

Cheng, G. D.: Problems on zonation of high-altitude permafrost, Ac. Geogr. Sin., 39, 185-193, 1984.

Cheng, G. D. and Wu, T. H.: Responses of permafrost to climate change and their environmental significance, Qinghai-Tibet Plateau, J. Geophys. Res., 112, F02S03, doi:10.1029/2006JF000631, 2007.

China Meteorological Administration.: The ground meteorological observation specification, China Meteorological Press, Beijing, China, 2003.

Cohen, J.: A Coefficient of Agreement for Nominal Scales, Educ. Psychol. Meas., 20, 37-46, 1960.

Coll, C., Caselles, V., Galve, J. M., Valor, E., Niclòs, R., Sánchez, J. M., and Rivas, R.: Ground measurements for the validation of land surface temperatures derived from AATSR and MODIS data, Remote. Sens. Environ., 97, 288-300, 2005.

Gillespie, A.: Land Surface Temperature, Encyclopedia of Remote Sensing, NY: Springer New York, New York, 314-319, 2014.

Gruber, S.: Derivation and analysis of a high-resolution estimate of global permafrost zonation, The Cryosphere, 6, 221-233, 2012.

Guo, W., Liu, S., Yao, X., Xu, J., Shangguan, D., Wu, L., Zhao, J., Liu, Q., Jiang, Z., Wei, J., Bao, W., Yu, P., Ding, L., Li, G., Li, P., Ge, C., Wang, Y.: The second glacier inventory dataset of China (version 1.0). Cold and Arid Regions Science Data Center at Lanzhou, 2014.

Hachem, S., Allard, M., and Duguay, C.: Using the MODIS land surface temperature product for mapping permafrost: an application to northern Québec and Labrador, Canada, Permafr. Perigl. Proc., 20, 407-416, 2009.

Haeberli, W., and Hohmann, R.: Climate, glaciers and permafrost in the Swiss Alps 2050: scenarios, consequences and recommendations, In Proceedings Ninth International Conference on Permafrost, 1, 607-612, 2008.

Huang, X., Deng, J., Wang, W., Feng, Q., and Liang, T.: Impact of climate and elevation on snow cover using integrated remote sensing snow products in Tibetan Plateau, Remote. Sens. Environ., 190, 274-288, 2017.

Jin, H., Wei, Z., Wang, S., Yu, Q., Lü, L., Wu, Q., and Ji, Y.: Assessment of frozen-ground conditions for engineering geology along the Qinghai-Tibet highway and railway, China, Eng. Geol., 101, 96-109, 2008.

Kääb, A.: Remote sensing of permafrost-related problems and hazards, Permafr. Perigl. Proc., 19, 107-136, 2008.

Kersten, M. S.: Laboratory research for the determination of the thermal properties of soils, ACFEL Technical Report, 23, AD 712516, 1949.

Klene, A. E., Nelson, F. E., and Shiklomanov, N. I.: The N-factor in natural landscapes: variablility of air and soil-surface temperatures, Kuparuk river basin, Alaska, U.S.A., Arct. Antarct. Alp. Res., 33, 140-148, 2001.

Langer, M., Westermann, S., and Boike, J.: Spatial and temporal variations of summer surface temperatures of wet polygonal tundra in Siberia - implications for MODIS LST based permafrost monitoring, Remote. Sens. Environ. 114, 2059-2069, 2010.

Lehnert, L., Meyer, H., Wang, Y., Miehe, G., Thies, B., Reudenbach, C., and Bendix, J.: Retrieval of grassland plant coverage on the Tibetan Plateau based on a multi-scale, multi-sensor and multi-method approach, Remote. Sens. Environ. 164, 197-207, 2015.

Li, K., Chen, J., Zhao, L., Zhang, X. M., Pang, Q. Q., Fang, H. B., and Liu, G. Y.: Permafrost distribution in typical area of west Kunlun Mountains derived from a comprehensive survey, Journal of Glaciology and Geocryology, 34(2), 447-454, 2012 (in Chinese).

Li, S. and Cheng, G.: Map of Frozen Ground on Qinghai-Xizang Plateau, Gansu Culture Press, Lanzhou, 1996.

Li, W., Zhao, L., Wu, X., Wang, S., Nan, Z., Fang, H., and Shi, W.: Distribution of Soils and Landform Relationships in Permafrost Regions of the Western Qinghai-Xizang (Tibetan) Plateau, China, Soil. Sci., 179, 348-357, 2014.

Li, W., Zhao, L., Wu, X., Wang, S., Sheng, Y., Ping, C., Zhao, Y., Fang, H., and Shi, W.: Soil distribution modeling using inductive learning in the eastern part of permafrost regions in Qinghai-Xizang (Tibetan) Plateau, Catena., 126, 98-104, 2015a.

Li, W., Zhao, L., Wu, X., Zhao, Y., Fang, H., and Shi, W.: Distribution of soils and landform relationships in the permafrost regions of Qinghai-Xizang (Tibetan) Plateau, Chin. Sci. Bull., 60, 2216-2226, 2015b.

Li, X.: The cryosphere information system and its application research, Lanzhou Institute of Glaciology and Geocryology, Chinese Academy of Sciences, 99p, 1998.

Li, X., and Cheng, G.: A GIS-aided response model of high-altitude permafrost to global change, Sci. China. Ser. D., 42, 72-79, 1999.

Li, X., Cheng, G., Jin, H., Kang, E., Che, T., Jin, R., Wu, L., Nan, Z., Wang, J., and Shen, Y.: Cryospheric Change in China, Global. Planet. Change., 62, 210-218, 2008.

Li, X., Cheng, G., and Lu, L.: Comparison study of spatial interpolation methods of air temperature over Qinghai-Xizang Plateau, Plateau Meteorology, 22, 565-573, 2003 (in Chinese).

Lin, Z., Niu, F., Liu, H., and Lu, J.: Hydrothermal processes of Alpine Tundra Lakes, Beiluhe Basin, Qinghai-Tibet Plateau, Cold. Reg. Sci. Technol., 65, 446-455, 2011.

Lin, Z. H., Mo, X. G., Li, H. X., and Li, H. B.: Comparison of Three Spatial Interpolation Methods for Climate Variables in China, Ac. Geogr. Sin., 1, 005, 2002.

Lunardini, V. J.: Theory of n-factors and correlation of data, In Proceedings of Third International Conference on Permafrost, 1, 40-46, 1978.

Nan, Z., Li, S., and Liu, Y.: Mean annual ground temperature distribution on the Tibetan Plateau: permafrost distribution mapping and further application, Journal of Glaciology and Geocryology, 24, 142-148, 2002 (in Chinese).

Nguyen, T. N., Burn, C. R., King, D. J., and Smith, S. L.: Estimating the extent of near-surface permafrost using remote sensing, Mackenzie Delta, Northwest Territories, Permafr. Perigl. Proc., 20, 141-153, 2009.

Niu, F., Lin, Z., Liu, H., and Lu, J.: Characteristics of thermokarst lakes and their influence on permafrost in Qinghai-Tibet Plateau, Geomorphology., 132, 222-233, 2011.

Nelson, F., and Outcalt, S.: A Frost Index Number for Spatial Prediction of Ground-Frost Zones. In: Permafrost-Fourth International Conference Proceedings, vol 1 Washington, DC: National Academy Press, 907-911, 1983.

Pang, Q., Zhao, L., Li, S., and Ding, Y.: Active layer thickness variations on the Qinghai-Tibet Plateau under the scenarios of climate change, Environ. Earth. Sci., 66, 849-857, 2011.

Prince, S. D., Goetz, S. J., Dubayah, R. O., Czajkowski, K. P., and Thawley, M.: Inference of surface and air temperature, atmospheric precipitable water and vapor pressure deficit using Advanced Very High-Resolution Radiometer satellite observations: comparison with field observations, J. Hydrol, 212, 230-249, 1998.

Pu, Z., Xu, L., and Salomonson, V. V.: MODIS/Terra observed seasonal variations of snow cover over the Tibetan Plateau, Geophys. Res. Lett., 34, L06706, 2007.

Qin, D., Liu, S., and Li, P.: Snow cover distribution, variability, and response to climate change in western China, J. Climate, 19(9), 1820-1833, 2006.

Qin, Y., Wu, T., Li, R., Xie, C., Qiao, Y., Chen, H., Zou, D., and Zhang, L.: Application of ERA Product of Land Surface Temperature in Permafrost Regions of Qinghai-Xizang Plateau, Plateau Meteorology, 34, 666-675, 2015 (in Chinese).

Qiu, G.Q.: The principle of geocryological regionalization and the compilation of frozen ground map. In *Geocryology in China*, Zhou YW, Guo DX, Qiu GQ, Cheng GD, Li SD (eds), Science Press, Beijing, 162-170, 2000, (in Chinese).

Qiu, J.: China: the third pole. Nature News, 454(7203), 393-396, 2008.

Ran, Y., Li, X., Cheng, G., Zhang, T., Wu, Q., Jin, H., and Jin, R.: Distribution of Permafrost in China: An Overview of Existing Permafrost Maps, Permafr. Perigl. Proc., 23, 322-333, 2012.

Riseborough, D.: The effect of transient conditions on an equilibrium permafrost-climate model, Permafr. Perigl. Proc., 18, 21-32, 2007.

Riseborough, D., Shiklomanov, N., Etzelmüller, B., Gruber, S., and Marchenko, S.: Recent advances in permafrost modelling, Permafr. Perigl. Proc., 19, 137-156, 2008.

Roerink, G. J., Menenti, M., and Verhoef, W.: Reconstructing cloudfree NDVI composites using Fourier analysis of time series, Int. J. Remote. Sens., 21, 1911-1917, 2000.

Romanovsky, V., Burgess, M., and Smith, S.: Permafrost Temperature Records: Indicators of Climate Change, EOS Transactions, American Geophysical Union, 83, 589-594, 2002.

Romanovsky, V., Smith, S., Christiansen, H.: Permafrost thermal state in the polar Northern Hemisphere during the international polar year 2007-2009: a synthesis, Permafr. Perigl. Proc., 21(2), 106-116, 2010.

Sheng, Y., Cao, Y. B., Li, J., Wu, J. C., Chen, J., and Feng, Z. L.: Characteristics of Permafrost along Highway G214 in the Eastern Qinghai-Tibet Plateau. Journal of Mountain Science, 12(5), 1135-1144, 2015.

585   Shi, Y., and Mi, D.: Map of snow, ice and frozen ground in China (1: 4 000 000), Beijing, China, Cartographic Publishing House, 1988 (in Chinese).

Smith, M. W., and Riseborough, D. W.: Permafrost Monitoring and Detection of Climate Change, Permafr. Perigl. Proc., 7, 301-309, 1996.

Smith, M. W., and Riseborough, D. W.: Climate and the limits of permafrost: a zonal analysis, Permafr. Perigl. Proc., 13,

590   1-15, 2002.

Smith, S. L., Burgess, M. M., Riseborough, D., and Mark Nixon, F.: Recent trends from Canadian permafrost thermal monitoring network sites, Permafr. Perigl. Proc., 16(1), 19-30, 2005.

Smith, S. L., Romanovsky, V. E., Lewkowicz, A. G., Burn, C. R., Allard, M., Clow, G. D., Yoshikawa, K., and Throop, J.: Thermal state of permafrost in North America: a contribution to the international polar year, Permafr. Perigl. Proc.,

595   21(2), 117-135, 2010.

Tong, B., and Li, S.: The mapping principles and method of the permafrost distribution along the Qinghai-Xizang (Tibetan) Plateau (1:600 000), In: Proceedings of the Second Chinese Permafrost Conference, Lanzhou, Gansu People Press, 75-80, 1983.

Wan, Z.: New refinements and validation of the MODIS land-surface temperature/emissivity products, Remote. Sens.

600   Environ., 112, 59-74, 2008.

Wan, Z.: Collection-5 MODIS Land Surface Temperature Products Users' Guide. http://www.icess.ucsb.edu/modis/LstUsrGuide/MODIS_LST_products_Users_guide_C5.pdf, 10-20, 2009.

Wan, Z., and Dozier, J.: A generalized split-window algorithm for retrieving land-surface temperature from space, IEEE. T. Geosci. Remote., 34, 892-905, 1996.

605   Wan, Z., Li, Z.: Radiance-based validation of the V5 MODIS land-surface temperature product, Int. J. Remote. Sens., 29, 5373-5395, 2008.

Wan, Z., Zhang, Y., Zhang, Y., and Li, Z.: Validation of the land-surface temperature products retrieved from Moderate Resolution Imaging Spectroradiometer data, Remote. Sens. Environ., 83, 163-180, 2002.

Wan, Z., Zhang, Y., Zhang, Y., and Li, Z.: Quality assessment and validation of the global land surface temperature, Int.

610   J. Remote. Sens., 25, 261-274, 2004.

Wang, T., Wang, N., and Li, S.: Map of the glaciers, frozen ground and desert in China, 1 : 4,000,000, Chinese Map Press, Beijing, China, 2006.

Wang, W., Rinke, A., Moore, J. C., Cui, X., Ji, D., Li, Q., Zhang, N., Wang, C., Zhang, S., Lawrence, D. M., McGuire, A. D., Zhang, W., Delire, C., Koven, C., Saito, K., MacDougall, A., Burke, E., and Decharme, B.: Diagnostic and

615   model dependent uncertainty of simulated Tibetan permafrost area. The Cryosphere, 10, 287-306, 2016.

Wang, Z., Wang, Q., Zhao, L., Wu, X., Yue, G., Zou, D., Nan, Z., Liu, G., Pang, Q., Fang, H., Wu, T., Shi, J., Jiao, K., Zhao, Y., and Zhang, L.: Mapping the vegetation distribution of the permafrost zone on the Qinghai-Tibet Plateau. J. Mt. Sci., 13(6), 1035-1046, 2016.

Wang, Z., Nan, Z., and Zhao, L.: The Applicability of MODIS Land Surface Temperature Products to Simulating the

620   Permafrost Distribution over the Tibetan Plateau, Journal of Glaciology and Geocryology, 33, 132-143, 2011 (in

Chinese).

Westermann, S., Langer, M., and Boike, J.: Spatial and temporal variations of summer surface temperatures of high-arctic tundra on Svalbard - Implications for MODIS LST based permafrost monitoring, Remote. Sens. Environ., 115(3), 908-922, 2011.

625 Westermann, S., Langer, M., and Boike, J.: Systematic bias of average winter-time land surface temperatures inferred from MODIS at a site on Svalbard, Norway, Remote. Sens. Environ., 118, 162-167, 2012.

Westermann, S., Østby, T., Gisnås, K., Schuler, T., and Etzelmüller, B.: A ground temperature map of the North Atlantic permafrost region based on remote sensing and reanalysis data, The Cryosphere, 9, 1303-1319, 2015.

Wu, Q., and Liu, Y.: Ground temperature monitoring and its recent change in Qinghai-Tibet Plateau, Cold. Reg. Sci.

630 Technol., 38, 85-92, 2004.

Wu, Q., Zhang, T.: Recent permafrost warming on the Qinghai-Tibetan Plateau, J. Geophys. Res., 113, D13, 2008.

Wu, Q., Zhu, Y., and Liu, Y.: Application of the permafrost table temperature and thermal offset forecast model in the Tibetan Plateau, Journal of Glaciology and Geocryology, 24, 614-617, 2002a (in Chinese).

Wu, Q., Zhu, Y., and Liu, Y.: Evaluation model of permafrost thermal stability and thawing sensibility under engineering

635 activity, Cold. Reg. Sci. Technol., 34, 19-30, 2002b.

Wu, X., Zhao, L., Fang, H., Zhao, Y., Smoak, J. M., Pang, Q., and Ding, Y.: Environmental controls on soil organic carbon and nitrogen stocks in the high-altitude arid western Qinghai-Tibetan Plateau permafrost region, J. Geophys. Res. Biogeosci., 121, 176-187, 2016.

Xu, Y., Shen, Y., and Wu, Z.: Spatial and Temporal Variations of Land Surface Temperature Over the Tibetan Plateau

640 Based on Harmonic Analysis, Mt. Res. Dev., 33, 85-94, 2013.

Yang, M., Nelson, F. E., Shiklomanov, N. I., Guo, D., and Wan, G.: Permafrost degradation and its environmental effects on the Tibetan Plateau: A review of recent research, Earth-Sci. Rev., 103, 31-44, 2010.

Zhang, T., Barry, R. G., and Armstrong, R. L.: Application of Satellite Remote Sensing Techniques to Frozen Ground Studies, Polar Geography, 28, 163-196, 2004.

645 Zhang, T.: Influence of the seasonal snow cover on the ground thermal regime: An overview, Rev. Geophys., 43(4), 2005.

Zhang, X. M., Nan, Z. T., Wu, J. C., Du, E. J., Wang, T., and You, Y. H.: Modeling permafrost distribution in Wenquan Area over Qinghai-Tibet Plateau by using multivariate adaptive regression splines, Journal of Glaciology and Geocryology, 33(5), 1088-1097, 2011 (in Chinese).

Zhang, X. M., Sheng, Y., Zhao, L., Wu, J. C., Chen, J., Du, E. J., and You, Y. H.: Permafrost distribution using sub-

650 region classification and multivariate data in the Wenquan area over the Qinghai-Tibet Plateau, Scientia Geographica Sinica, 32(12), 1513-1520, 2012 (in Chinese).

Zhang, Y. L., Li, B. Y., Zheng, D.: A discussion on the boundary and area of the Tibetan Plateau in China, Geographical Research, 21(1), 1-9, 2002 (in Chinese).

Zhang, Y. L., Li, B. Y., Zheng, D.: Datasets of the boundary and area of the Tibetan Plateau. Global Change Research

655 Data Publishing and Repository, 2014. DOI: 10.3974/geodb.2014.01.12.v1, http://www.geodoi.ac.cn/WebEn/doi.aspx?doi=10.3974/geodb.2014.01.12.v1.

Zhao, L., Ping, C. L., Yang, D., Cheng, G., Ding, Y., and Liu, S.: Changes of climate and seasonally frozen ground over the past 30 years in Qinghai-Xizang (Tibetan) Plateau, China, Global. Planet. Change., 43, 19-31, 2004.

Zhao, L., Wu, Q., Marchenko, S. S., and Sharkhuu, N.: Thermal state of permafrost and active layer in Central Asia during the international polar year, Permafr. Perigl. Proc., 21, 198-207, 2010.

Zhou, Y., Guo, D., Qiu, G., Cheng, G., and Li, S.: China Permafrost, Science Press, Beijing, 145-151, 2000.

Zou, D., Zhao, L., Wu, T., Wu, X., Pang, Q., and Wang, Z.: Modeling ground surface temperature by means of remote sensing data in high-altitude areas: test in the central Tibetan Plateau with application of moderate-resolution imaging spectroradiometer Terra/Aqua land surface temperature and ground-based infrared radiometer, J. Appl. Remote. Sens., 8, 083516, 2014.

Table 1. Field survey samples statistics in five investigated regions

	Investigated Region (IR)					
	WQ	B-Q	AEJ	GZ	XKL	Total
Boreholes	21	40	13	23	28	125
Soil pits	74	55	/	19	51	199

670

675

Table 2. Soil thermal parameters of each type on the Tibetan Plateau

Soil order	Samples Number	Moisture content (%)	Bulk density (kg m^{-3})	thawed soil thermal conductivity (W m^{-1} K^{-1})	frozen soil thermal conductivity (W m^{-1} K^{-1})
Aridisols	43	7.76 ($\pm$3.0)	1601.9 ($\pm$173.2)	1.47 ($\pm$0.42)	1.25 ($\pm$0.63)
Entisols	10	8.79 ($\pm$6.64)	1447.7 ($\pm$164.8)	1.23 ($\pm$0.17)	1.01 ($\pm$0.33)
Gelisols	56	22.24 ($\pm$13.79)	1277.6 ($\pm$310.0)	1.22 ($\pm$0.36)	1.62 ($\pm$0.44)
Inceptisols	94	16.22 ($\pm$7.37)	1313.4 ($\pm$221.7)	1.18 ($\pm$0.34)	1.30 ($\pm$0.53)
Mollisols	14	20.00 ($\pm$5.66)	1186.9 ($\pm$141.3)	1.05 ($\pm$0.23)	1.22 ($\pm$0.48)

680

Table 3. Kappa coefficient statistics in five investigated regions of three maps

Investigated Region	TP-1996	TP-2006	TP-2016
WQ	0	0.77	0.78
B-Q	0	0.63	0.68
AEJ	0	0	0.38
GZ	0.15	0.19	0.48
XKL	0.14	0.17	0.54
Average	0.06	0.35	0.57

685

Table 4. Kappa coefficient statistics in three transects of three maps

Transect	TP-1996	TP-2006	TP-2016
G214	0.32	0.41	0.62
G109	0.21	0.59	0.69
G219	0.47	0.49	0.74
Average	0.34	0.50	0.68

690

Table 5. Kappa coefficient statistics among three maps

	TP-1996	TP-2006	TP-2016
TP-1996	1	0.56	0.53
TP-2006	/	1	0.71
TP-2016	/	/	1
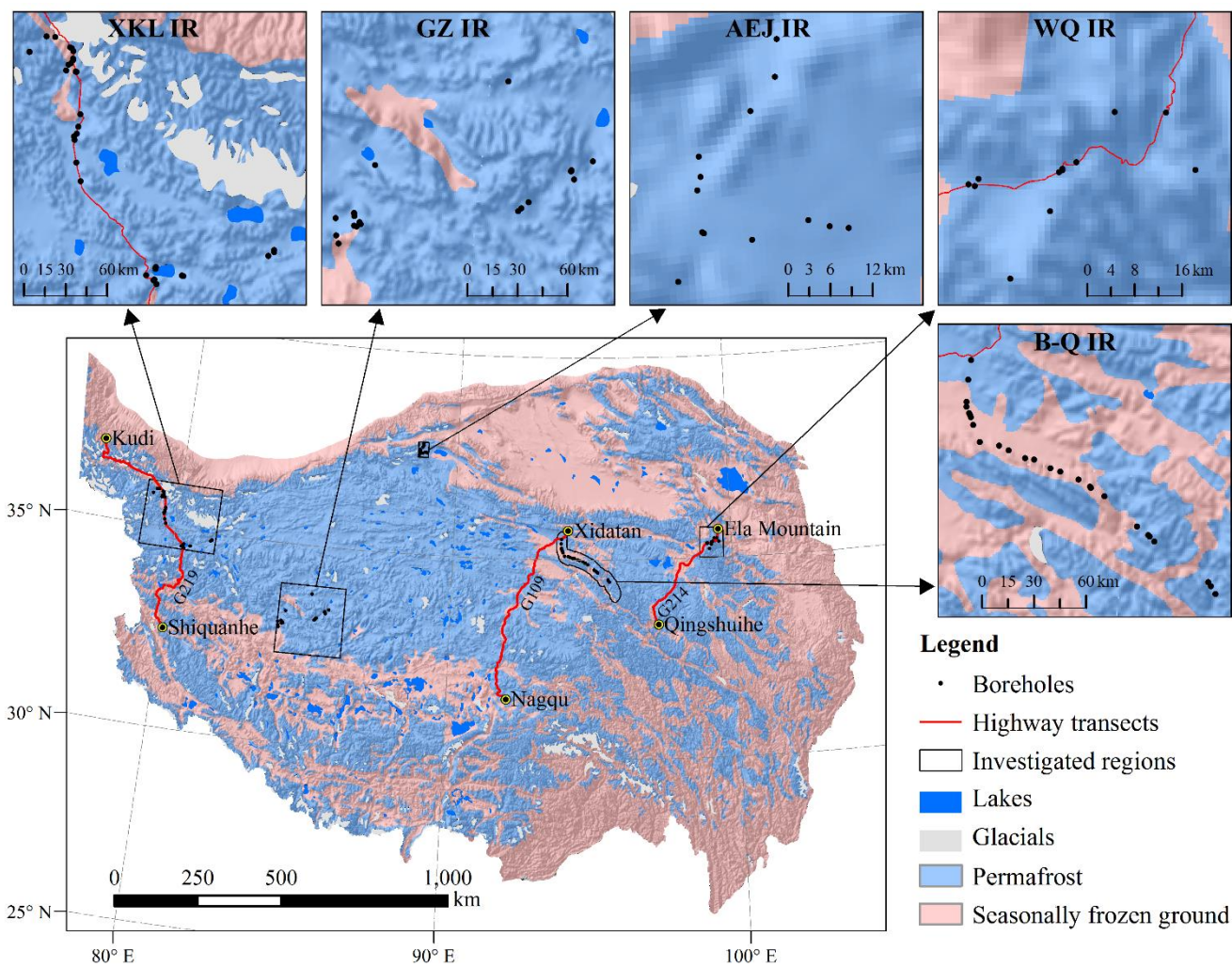
Figure 1. Spatial distribution of the field survey regions on the Tibetan Plateau (based on the permafrost distribution map made in 1996)
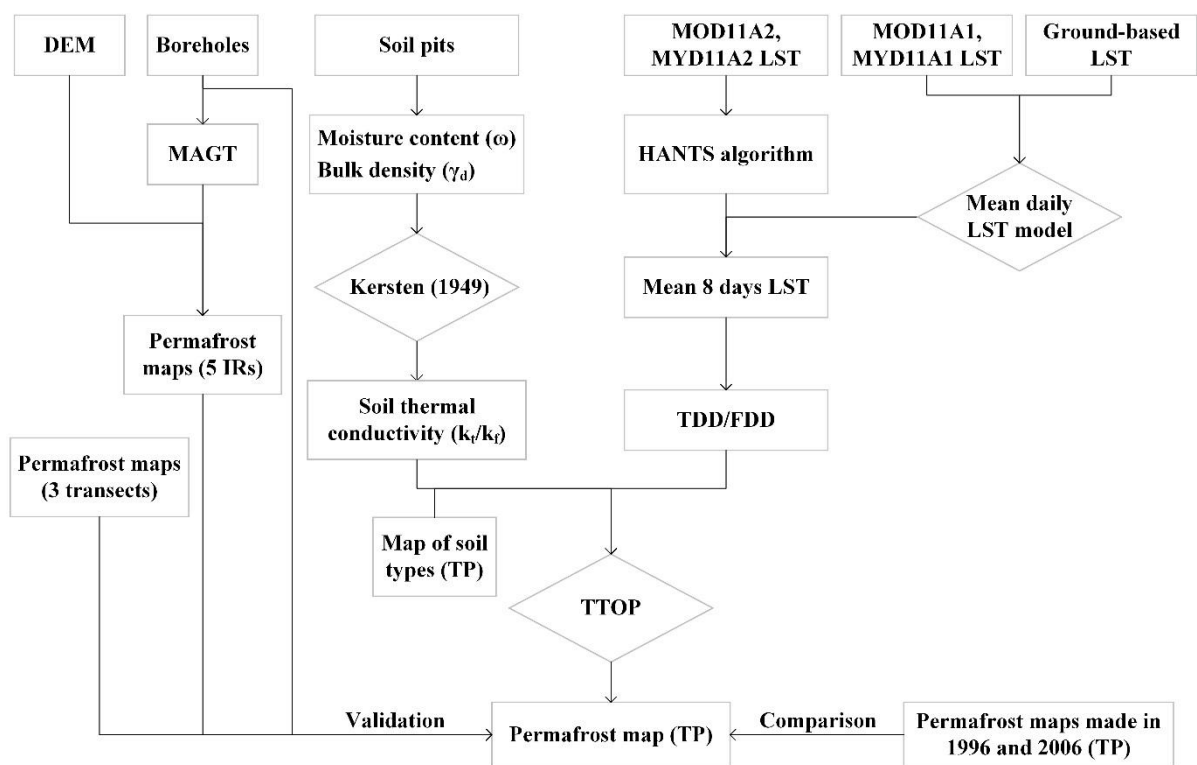
700 **Figure 2.** Flow diagram of the modelling scheme
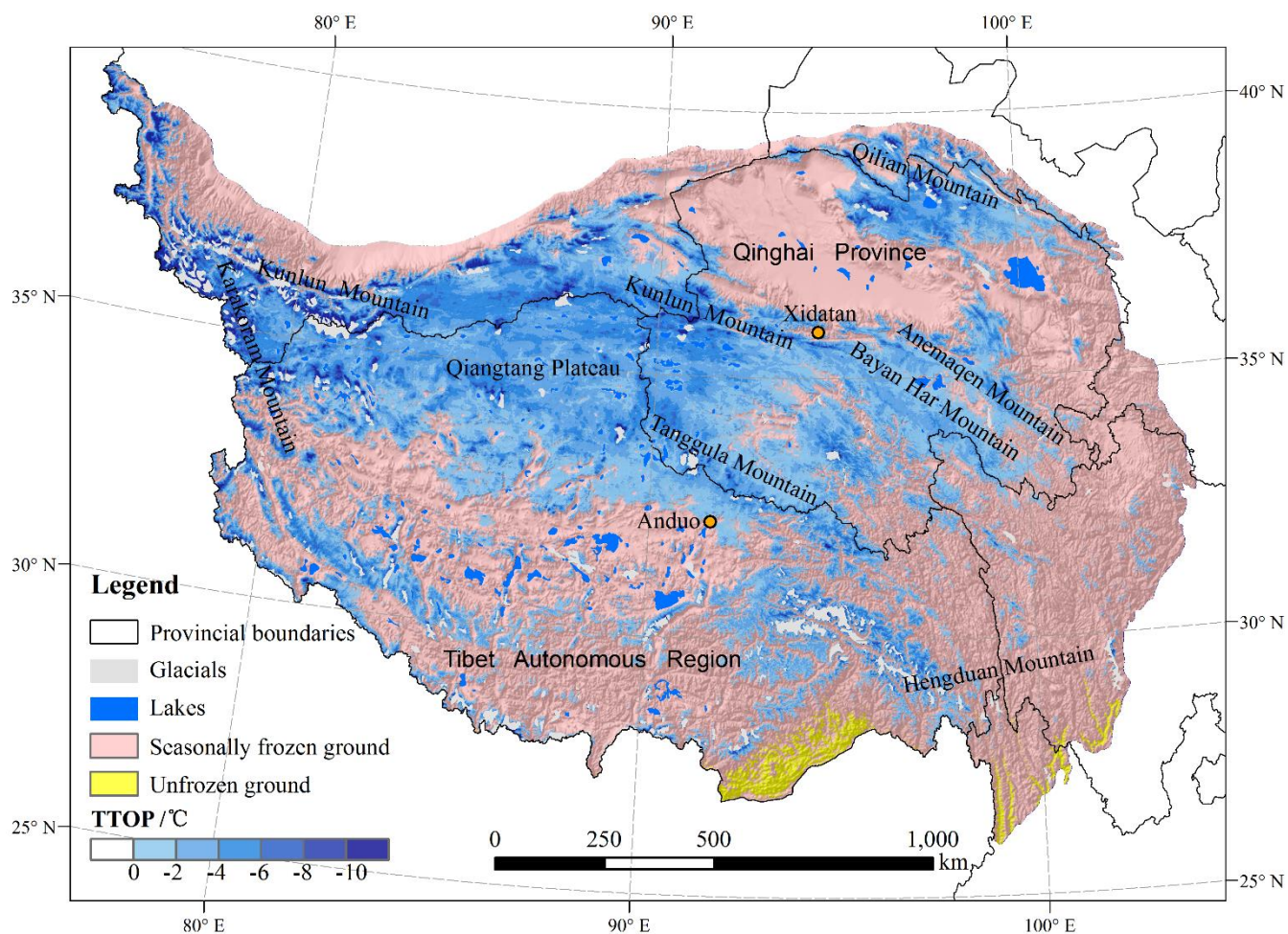
705 **Figure 3.** Spatial distribution of permafrost with the derived TTOP on the Tibetan Plateau
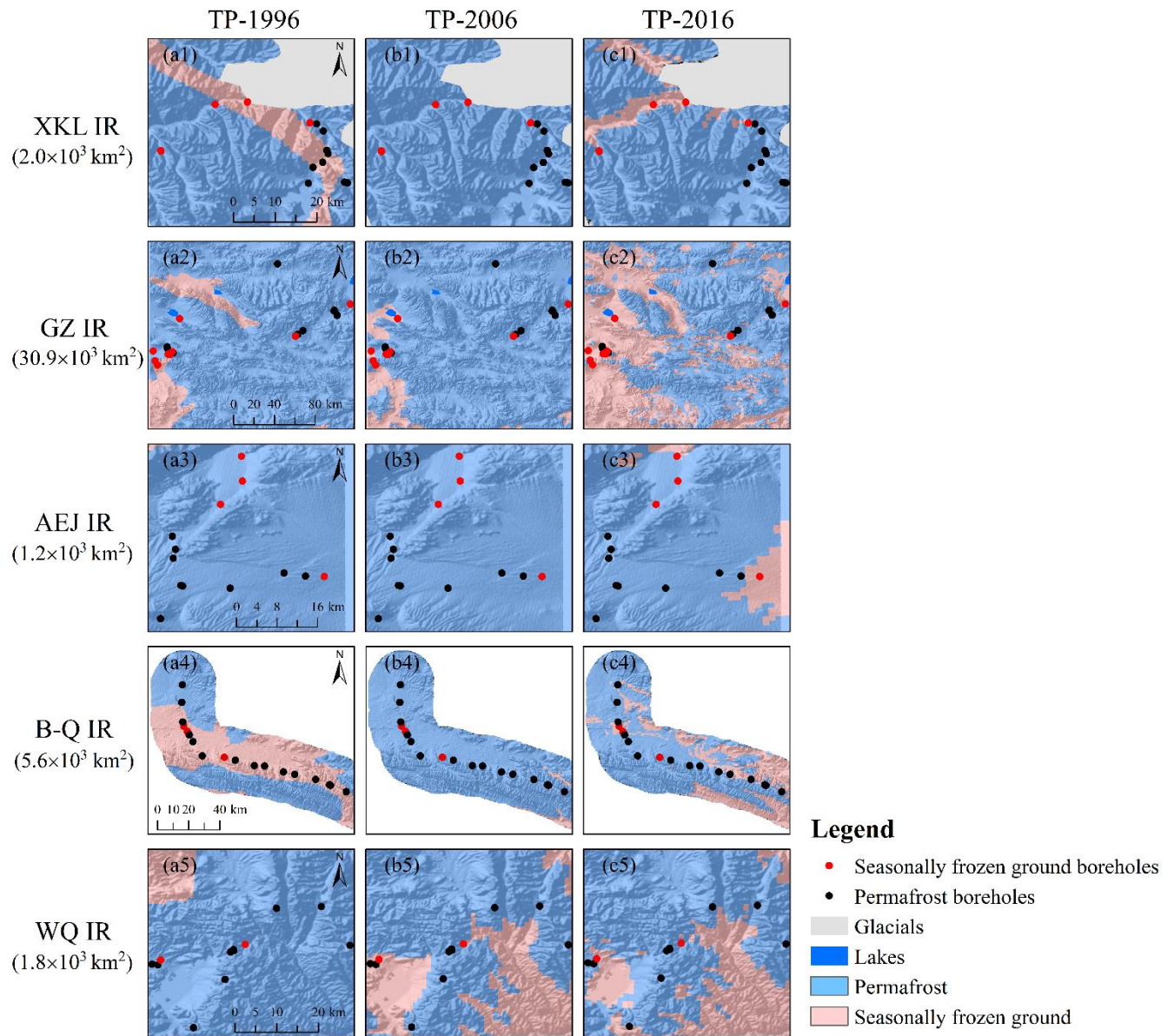
Figure 4. Spatial distribution of boreholes in five IRs of three maps
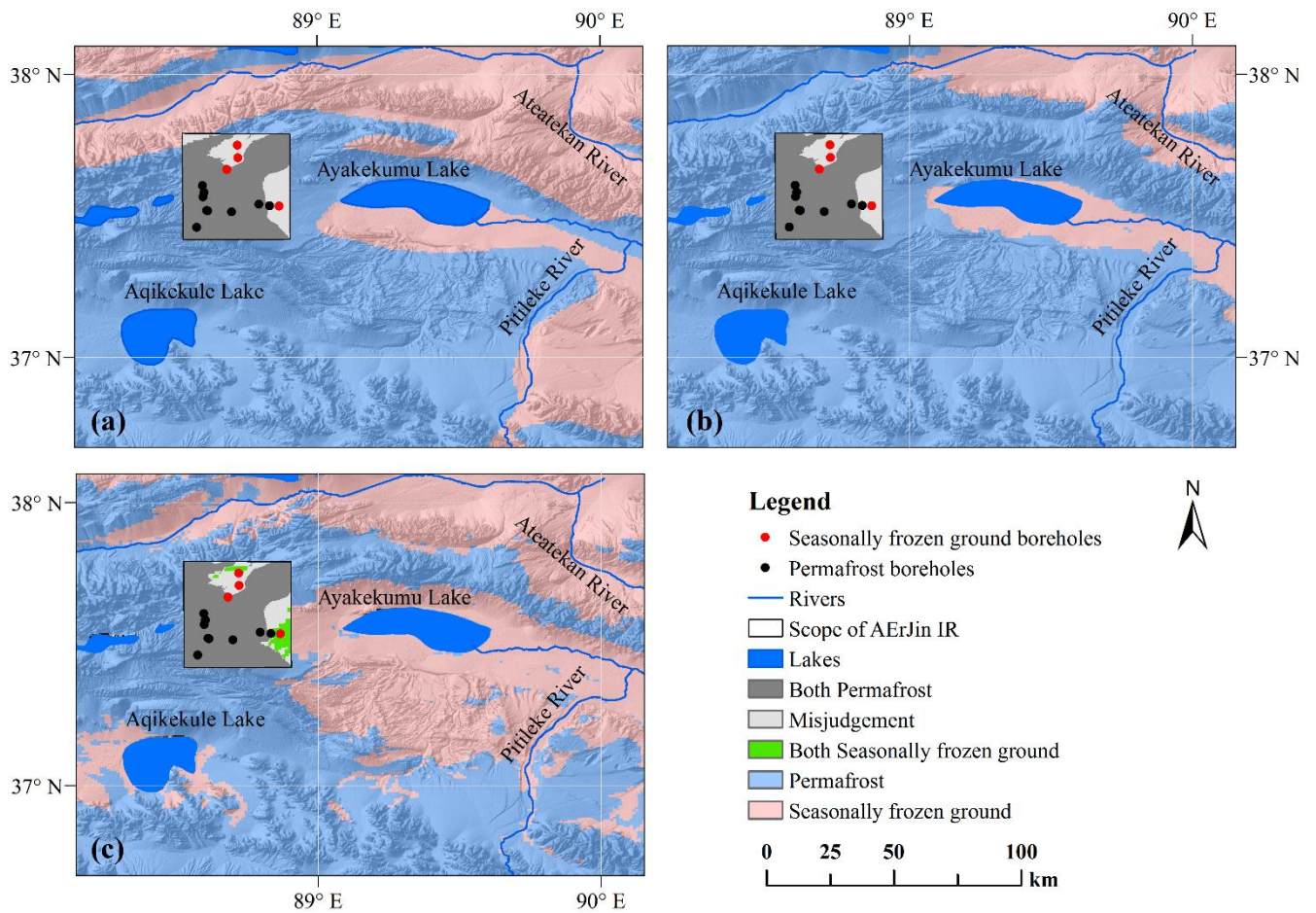
Figure 5. Comparison of the three maps in and around the AErJin investigated region (a: TP-1996; b: TP-2006; c: TP-2016)

715
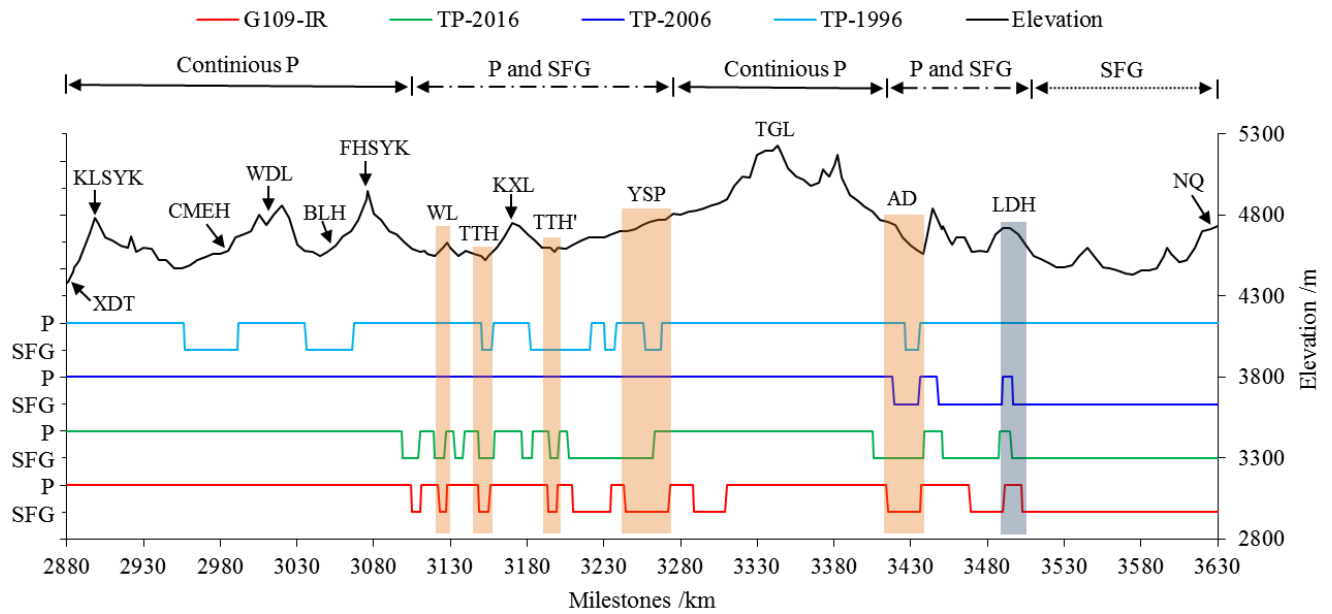
Figure 6. Comparison of permafrost distribution of three maps along the G109 transect with investigated result (P: permafrost, SFG: seasonally frozen ground; XDT: Xidatan, KLSYK: Kunlun Mountain Peak, WDL: Wudaoliang, BLH: Beilu River, FHSYK: Fenghuo Mountain Peak, WL: Wuli, TTH: Tuotuo River, KXL: Kaixin Mountain Ridge, TTH': Tongtian River, YSP: Yanshiping Town, TGL: Tangula Mountain Peak, AD: Anduo Town, LDH: Liangdaohe, NQ: Nagqu Town, G109-IR: investigated result of permafrost distribution in G109 transect)

725
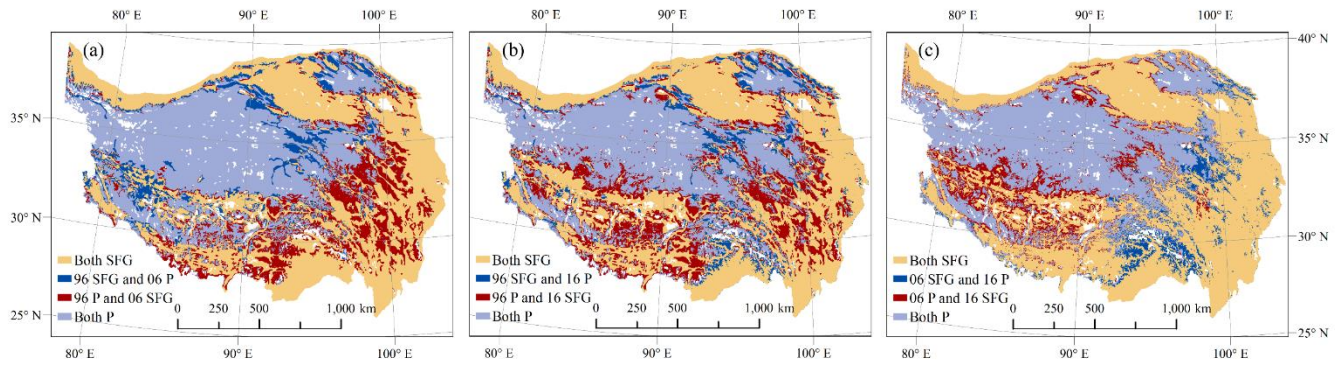
Figure 7. Spatial difference among the three maps (96: TP-1996, 06: TP-2006, 16: TP-2016; SFG: seasonally frozen ground, P: permafrost)
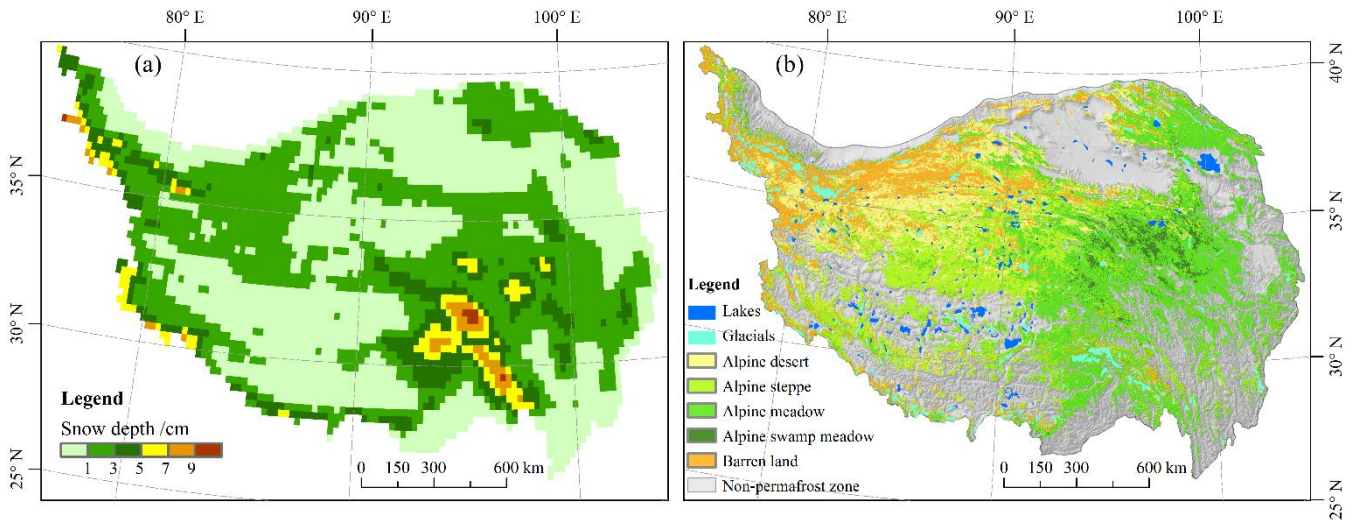
730

Figure 8. Annual average snow-depth (a; edited after Che et al., 2008) and vegetation types of the permafrost region (b; edited after Wang et al., 2016) on the Tibetan Plateau